Strong downdrafts preceding rapid tropopause ascent and their potential to identify cross-tropopause stratospheric intrusions

Feilong Chen[1], Gang Chen[1*], Chunhua Shi[2], Yufang Tian[3], Shaodong Zhang[1], Kaiming Huang[1]

[1]School of Electronic Information, Wuhan University, Wuhan 430072, China.

[2]Key Laboratory of Meteorological Disaster, Ministry of Education, Nanjing University of Information Science &Technology, Nanjing 210044, China.

[3]Key Laboratory of Middle Atmosphere and Global Environment Observation, Institute of Atmospheric Physics, Chinese Academy of Sciences, Beijing 100029, China

*Corresponding author: Gang Chen (g.chen@whu.edu.cn)

Abstract:

The capability of measuring 3-dimensional wind and tropopause structure with relatively high time and vertical resolution makes VHF radar a potentially significant tool for studying various processes of the atmosphere. Here the potential detection of stratospheric intrusion events is discussed using the Beijing MST radar located at Xianghe (39.75°N, 116.96°E). During the passage of a cut-off low in late November 2014, a deep V-shaped tropopause structure, and strong downdrafts (>0.8 m/s) immediately preceding the rapid tropopause ascent (>0.2 km/h) were observed. Within the height region of the downdrafts, the 'normal' radar-tropopause layer seems to be weakened. Analysis results from global reanalysis and the satellite data, as well as the

trajectory model have shown the clear evidence of the downward stratospheric intrusions (dry ozone-rich and depleted methane air) associated with the strong downdrafts. According to the previous studies and the present case observation, the strong downdrafts preceding rapid tropopause ascent are considered as a significant signature of stratospheric intrusions. Twenty typical cases of such strong downdrafts, occurring during various synoptic processes in different seasons, have been presented and 16 of them are exactly associated with some form of stratospheric intrusions. Four years (2012-2015) of such downdrafts are further discussed. The observations reveal that the strong downdrafts preceding the rapid tropopause ascent can be a valuable diagnostic for monitoring intrusion events, which will gain a better understanding of stratospheric intrusions in VHF radar observations.

Keywords: Stratospheric intrusions; strong downdrafts; rapid tropopause ascent; MST radar; VHF radar; cut-off low

1. Introduction

The tropopause is a stable transition zone separating the vertically stable stratified stratosphere from the active free troposphere. The stratospheric and tropospheric air are remarkably different in their chemical and dynamical characteristics. The stratosphere is dominantly high in ozone and potential vorticity (PV) content and low in water vapor (WV) and methane (CH_4) concentration, while the troposphere is just on the contrary (Holton et al., 1995). Consequently, the natural stable tropopause layer, characterized by strong gradients of trace constituents and wind speeds, plays an important role in stratosphere-troposphere exchange (STE) processes. In other words, the layer is a significant barrier for the atmospheric transport between stratosphere and troposphere (Mahlman, 1997). From a point of view, the long-term seasonal variation of the tropopause height determines the seasonal variation of the flux of stratospheric air into the free troposphere (Appenzeller et al., 1996). Under the global climate warming (e.g. the continuing rise in CO_2), the tropopause variation is also a significant factor that must be considered with regards to the recovery of the stratospheric ozone (Butchart et al., 2010; Chipperfield et al., 2017). On the other hand, the short-term tropopause variability is sensitive to various meso– and small–scale atmospheric processes, during which the folding/intrusion events commonly occur. This characteristic of the tropopause change are sometimes directly used to detect the tropopause folds (e.g. Rao et al., 2008; Alexander et al., 2012, and references therein), but are less, if any, directly used to identify stratospheric intrusions. More detailed analysis of the variability of high-resolution tropopause height and of course some other parameters (e.g. 3-

dimentional wind), and how the stratospheric air is transported across the tropopause into the troposphere will help us to yield better understanding of the downward stratospheric intrusions (e.g. Sprenger et al., 2003; Leclair de Bellevue et al., 2007; Das et al., 2016).

Although photochemical production within the troposphere is the main source of tropospheric ozone, the influence of the downward stratospheric intrusions on the tropospheric ozone content cannot be ignored (Oltmans and Levy II, 1992; Monks, 2000; Stevenson et al., 2006). Stratospheric intrusions bring dry ozone-rich air down into the free troposphere (e.g. Stohl et al., 2000; Sørensen and Nielsen, 2001) and sometimes even deep to the surface (e.g. Gerasopoulos et al., 2006; Ding and Wang, 2006; Lefohn et al., 2011). By now, it is well established that these intrusions of stratospheric origin will significantly influence other trace gases (such as hydroxyl (OH)) in the troposphere (Holton et al., 1995). These influences then will further contribute to the change of radiative balance (Ramaswamy et al., 1992) and play an important role in the radiative forcing of global climate change (Holton et al., 1995). It is true that stratospheric intrusion events occur all over the world and in any season. However, they are highly episodic in both vertical and isentropic (horizontal) directions (Chen, 1995). Various dynamical and physical processes have been proposed to be responsible for extra-tropical intrusion events. These mainly include tropopause folds, stratospheric streamers and break-up, cut-off lows (COLs), wave breaking, and mesoscale convective activities and thunderstorms (Stohl et al., 2003).

The certain dynamical and chemical characteristics of stratospheric air allow the

82 tracers, such as dry ozone-rich and high PV, to be proper indicators for the intrusions
83 penetrating down into the troposphere. Various methods are available to detect intrusion
84 events based on these tracers. Among them, balloon-borne ozonesonde sounding are
85 without doubt one of the most appropriate tools, but is limited by coverage (He et al.,
86 2011) and not possible to obtain continuous profiles with fine temporal resolution. In
87 contrast, the satellite-borne remote sensing instruments, such as Atmospheric Infrared
88 Sounder (AIRS), can provide nearly global coverage of various trace gases but have
89 limitations in vertical and temporal resolution. Another method for studying transport
90 processes is trajectory model, from which the backward trajectories can provide
91 valuable information on the possible sources of the trace gases (e.g. Elbern et al., 1997).
92 By far, large-scale STE has been widely studied and is fairly well understood, but
93 the details of small scale intrusions still remain uncertain (Holton et al., 1995). Kumar
94 and Uma (2009) reported that the dearth of direct vertical wind measurements in the
95 vicinity of the tropopause may be responsible for the lack of detailed fine observations
96 of smaller scale intrusions.
97 Very-High-Frequency (VHF) radars, compared to the tools mentioned above, are
98 capable to provide 3-dimensional wind and tropopause height continuously with both
99 high temporal and spatial resolution and can operate unmanned continuously for 24
100 hours per day under any weather conditions. During the past two decades, VHF radar
101 measurements were commonly used to assist to study the stratospheric intrusions.
102 However, it still remains uncertain in many aspects when using only the VHF radar to
103 identify intrusion events. Complicated and changeable atmospheric processes make it

104 difficult to identify the intrusion events by only radar data. The research by Hocking et
105 al., (2007) have achieved a development in this issue. They found that the rapid ascent
106 in radar tropopause altitude (>0.2 km/h) can be a valuable diagnostic for possible
107 stratospheric intrusions and the RT height started to ascent when the stratospheric air
108 just intruded across the tropopause layer. However, it does not always work (e.g. He et
109 al., 2011) and remains uncertain when purely using the information of radar-determined
110 tropopause.

111 The central objective of the present study is to discuss the signature of downward
112 cross-tropopause intrusions using both the measurements of tropopause height and
113 vertical wind by the Beijing MST radar. This study is carried out mainly via a detailed
114 case observation during the passage of a COL and other general cases associated with
115 various atmospheric processes. Our discussion mainly focused on the potential of the
116 MST radar data to identify possible intrusion events, which is the main point of this
117 paper. In section 2 the datasets used in this paper are described, section 3 presents
118 detailed results and discussion, and section 4 gives the conclusions.

119

2. Dataset

2.1. MST radar data and tropopause detection

The Beijing MST radar located at Xianghe, China (39.75° N, 116.96° E, 22 m above sea level) is a VHF radar operated at 50 MHz and installed in 2010 based on the first phase of Chinese Meridian Space Weather Monitoring Project (Chinese Meridian Project for short) (Wang, 2010). The radar antenna array consists of 24×24 three-element Yagi to produce an average power aperture product of 3.2×10^8 Wm^2 and maximum directive gain of 34.8 dB. It operates radiation pattern with 172 kW peak power and 3.2° half-power beam width. More detailed information of the radar system can be found in Chen et al. (2016). Routine low mode data were used for present study with 0.5 h time resolution and 1 μs coded pulse, which provides 150 m vertical resolution. Details of the low mode setup used in this study are given in Table 1.

It has long been known that VHF radar reflectivity is proportional to the mean generalized refractive index gradient M, which is a function of humidity variation and static stability and given by (Ottersten, 1969) as follows

$$M = -77.6\times10^{-6}(p/T)(dln\theta/dz) \cdot\{1+15500q/T[1-(dlnq/dz)/\ (2dln\theta/dz)]\ \} \quad (1)$$

where p is the atmospheric pressure (hPa) T is the temperature (K), θ is the potential temperature (K) and q is the specific humidity (gg^{-1}). According to the second and third terms of the equation (1): large humidity variation contributes to the echo from the lower and middle troposphere. From the first term: the radar backscatter power is proportional to the static stability, which in fact is directly proportional to the potential

142 temperature gradient. The tropopause, near which a strong potential temperature
143 gradient exists, will lead to strong radar echoes in vertical incidence, as well as large
144 radar aspect sensitivity (as shown in Figure 1). Radiosonde data used in this paper were
145 received from the GTS1 type digital radiosonde launched from Beijing Meteorological
146 Observatory (39.93 ºN,116.28 ºE, station number 54511), which is less than 45 km
147 away from the MST radar site. The black line in Fig.1 denotes the lapse-rate tropopause
148 (LRT) defined using the temperature lapse rate (World Meteorological Organization
149 (WMO), 1986). Applying the characteristic (enhanced radar echoes due to partial
150 specular reflection) mentioned above, the tropopause can be detected and its height
151 determined by VHF radars (Gage and Green, 1979). It has received widespread
152 application around the world, either in middle latitudes (e.g. Hocking et al., 2007), polar
153 regions (e.g. Alexander et al., 2012), and tropical regions (e.g. Yamamoto et al., 2003;
154 Das et al., 2008). Here, the radar-determined tropopause (RT) height is defined as the
155 height (above 500 hPa) where the maximum vertical gradient of echo power located
156 (shown as the orange circle in Figure 1a). This definition of RT is similar to that in the
157 studies of Alexander et al., 2012 and Ravindrababu et al., 2014.

158 In the present study, the MST radar mainly provides continuous measurements of
159 backscattered echo power, 3-D wind, and RT height with time resolution of 0.5 hour. In
160 addition, the radar aspect sensitivity, expressed as the ratio between vertical (p_v) and
161 oblique (p_o) beam echo power, is mainly caused by the horizontally stratified
162 anisotropic stable air and thus will be used as potential signature of stratospheric
163 intrusions in the troposphere (e.g. Kim et al., 2001). The backscattered echo power

given here is expressed as relative power in decibels (dB). In order to reduce the random noise, the profile of p_v is smoothed by a 3-point running mean in altitude. Note that the data that are heavily contaminated will be eliminated from our datasets. The data of Dec. 2015 and Sep. 2015 are excluded.

2.2. AIRS satellite data

The AIRS instrument on NASA Aqua/EOS polar orbit satellite is a 2378 channel nadir cross-track scanning infrared spectrometer. It can provide profiles of a number of trace gases, including ozone and CH_4 (Susskind et al., 2003). The footprint of these retrieval data is of 45 km by 45 km and their most sensitive region is in an altitude range of 300-600 hPa. Many studies have shown that these AIRS retrieval constituents are useful indicators for detecting stratospheric intrusions. He et al. [2011] suggested that AIRS can observe the enhanced tropospheric ozone that is of stratospheric origin. Xiong et al. [2013] reported that AIRS is capable of observing abnormal depletion in CH4 in the troposphere during intrusions. AIRS offers good latitude-longitude coverage. Here we use version 6 of the AIRS Level-3 ozone and methane retrieval products.

2.3. Meteorological reanalysis

European Centre for Medium-Range Weather Forecasts (ECMWF) reanalysis ERA-interim data are also used. After Nov. 2000 the data are based on the T511L60 version available with a 6-h temporal resolution and $3^o \times 3^o - 0.125^o \times 0.125^o$ latitude-longitude grid. The dataset from 15 isentropic and 37 pressure levels interpolated into $0.5^o \times 0.5^o$ grid are applied for present study.

2.4. HYSPLIT model

186 Backward (forward) trajectories in given starting locations are capable to
187 reproduce the sources (destinations) of the air parcel that will allow us to examine the
188 intrusions of stratospheric origin in the troposphere (e.g. Elbern et al., 1997). The
189 Hybrid Single Particle Lagrangian Integrated Trajectory model (HYSPLIT) developed
190 by the National Oceanic and Atmospheric Administration (NOAA)'s Air Resource
191 Laboratory (ARL) (Rolph, 2003; Stein et al., 2016) is applied to calculate the backward
192 and forward trajectories. The calculation method of the model is a hybrid between the
193 Lagrangian approach and the Eulerian methodology. In this paper, Global Data
194 Assimilation System (GDAS) datasets are adopted for driving the HYSPLIT.
195

3. Results and discussion

3.1. Meteorological synoptic situation

On the morning of 29 November 2014, a 500-hPa trough developed on the western side of Lake Baikal (Western Siberia). The trough moved southeastward and extended equatorward and its southern tip separated from the westerlies in the afternoon of 30 November 2014 (Fig. 2b), forming a COL near the radar site as shown by the closed geopotential contour. The black stars in Figure 1 and other figures indicate the location of the radar site. On the following days, the COL system moved northeastward gradually (Fig. 2b) and finally stayed over eastern Russia near Sakhalin Island until it reconnected and merged to the westerly flow. 315 K isentropic PV patterns have shown the coarse resolution features of intrusions from the polar reservoir across the tropopause into the midlatitude troposphere. The PV streamer curved and rolled up cyclonically along the western flank of the COL (Fig.2b).

Fig. 3 shows the time series of hourly surface meteorological parameters over the Beijing station. The data are obtained from the Chinese National Meteorology Information Center and is less than 50 km from the MST radar site. As the dry-cold air invasion accompanied with the COL travelled deeply into the planetary boundary layer, it brought severe weather to the surface, including a rapid decrease in temperature and humidity, and rapid increase in surface wind and sea level pressure. The humidity decreased from ~85 to 12 percent within less than 8 hours. It is well established that the polar-type COLs have strong potential to trigger deep convection (Price and Vaughan, 1993). To examine the potential convection, maps of high quality Climate Data Record

(CDR) of daily Outgoing Longwave Radiation (OLR) are displayed in Fig. 4. During the development of the COL, a local region with abnormal low OLR value was clearly observed near the radar site on 29 Nov. (Fig. 4b). The Satellite-observed cloud top temperature also showed the low values corresponding to the low OLR (figure not shown), indicating that convection may be generated near radar side on 29 Nov.. Please note that we did not observe such low value either in OLR (Fig.4c, d) or in cloud top temperature near the radar side on 30 Nov. and 1 Dec.. The time for all the observations in this paper is shown in Universal Time (UTC) which is eight hours behind Beijing standard time (LT=UTC+8).

3.2. MST radar observations

Radar echo power, horizontal wind vector, vertical wind, and radar aspect sensitivity are plotted in Figure 5 as function of height and time during the passage of the COL. Time variation of RT (black line) and LRT (black crosses) heights are also displayed. The RT height first experienced a rapid descent, and then increased rapidly, forming a deep V-shaped structure of ~4 km depth. The vertical velocity of the RT height variation (both the rapid descent and ascent branches) reaches up to 0.28 km/h. The rapid RT variation in altitude is in fact the response of the tropopause fold below the jet stream, which will be well represented in Fig. 8a. Rapid variation in RT height remained a region with low echo power (marked by R on Fig. 5a) and low aspect sensitivity (marked by R' on Fig. 5d) where they should be normally high value within the 'normal' tropopause layer. Unlike the RT height, the radiosonde LRT altitudes are nearly constant during the COL passage. In normal conditions, RT agrees well with the

LRT altitude, such as indicated by Fig. 6a. However, large differences, of order of 2.5 km (as shown in Fig.6b at 12 UTC 30 Nov.), are observed between LRT and RT in altitude during the passage of the COL as expected. It is the difference in definition that contribute most to the large differences, especially under the tropopause fold conditions. It is worth noting that, in Fig.6b, although there is no clear reversion in the radiosonde temperature profile within the height of RT, the RT height exactly corresponds well to the reversion of zonal and meridional wind and potential temperature gradient. Such differences between RT and LRT heights can commonly be observed, especially during extreme synoptic situations such as cyclone (e.g. Alexander et al., 2012).

The most important observation in this detailed case experiment is the strong downdrafts (hereinafter inferred to as main downdrafts) observed immediately preceding the rapid RT ascent (Fig.5c). The radar echo power sharply weakened (dotted rectangle in Fig.5a) and the wind direction changed rapidly (Fig.5b, change from dominant southerly wind to dominant northerly jet) within the height region of the main downdrafts. As mentioned previously, abnormal low value in OLR and cloud top temperature indicates the possible occurrence of convective activity on 29 Nov., but nothing special appeared on 30 Nov. near radar site. Consequently, we preliminarily consider that the main downdrafts occurred near 07 UT 30 November might not be produced directly by convective activity. Here, the accurate origin of the main downdrafts will not be discussed in detail, and it is also beyond the scope of present study.

The research by Hocking et al. (2007) has suggested that the rapid RT ascent (>0.2

262 km h^{-1}) can be a valuable indicator for the occurrence of stratospheric intrusions. Here
263 in this paper, the main downdrafts preceding the rapid RT ascent observed by the
264 Beijing MST radar are thus suspected to be an important feature or response of some
265 form of vertical stratospheric intrusions. Firstly, as the tropopause descends (folded
266 downward), it will displace stratospheric air into the troposphere (e.g. Hoskins et al.,
267 1985). Secondly, the main downdrafts will act as an effective way to weaken the
268 tropopause by means of continuously impinging on the tropopause, through which the
269 stratospheric air is permitted to penetrate down into the free troposphere (e.g.
270 Hirschberg and Fritsch, 1993; Kumar, 2006). In addition, after the main downdrafts,
271 the observed region near the upper troposphere with strong backscatter echoes (marked
272 by Q) and especially with abnormal high aspect sensitivity (marked by Q') may also be
273 a weak signature of the possible intrusions. In normal conditions in the upper-
274 troposphere, they are usually low in value (such as the region marked by P and P'). As
275 we mentioned before, the large value in radar aspect sensitivity is mainly caused by
276 reflection from stable atmospheric layer, such as the tropopause or lower-stratosphere.
277 When stable stratospheric air intrudes into the troposphere and without mixing with the
278 surrounding air mass, the intrusions in the free troposphere will be reflected as
279 abnormal large aspect sensitivity. Further direct evidence of the relevant intrusions in
280 dynamical and chemical aspects will be demonstrated in next section, using satellite
281 AIRS and global reanalysis data.

282 3.3. Associated stratospheric intrusions

283 Due to the sensitivity of the AIRS retrieved ozone and CH_4 is between 300-600

hPa. Fig. 7 shows the 500 hPa distribution of AIRS observed ozone and CH_4, along with the AIRS tropopause contour (defined based on the temperature lapse-rate). The ozone distribution maps (left panels of Fig. 7) clearly show a large area with enhanced tropospheric ozone (>80 ppbv) near the radar site during the passage of the COL. Moreover, severe CH_4 depletion (<1840 ppbv) was also observed (right panels in Fig.8). These features of the ozone enhancement, CH_4 depletion, and the corresponding low tropopause altitude clearly support the evidence of vertical downward cross-tropopause stratospheric intrusions on 30 Nov..

The vertical cross-section of ECMWF PV and specific humidity at 1800 UT 30 November 2014 and the daily AIRS ozone on 30 November 2014, along a constant latitude 40° N, is shown in Fig. 8. The corresponding vertical structure of the stratospheric intrusions (dry ozone-rich and high PV along with low tropopause) over regions near radar side is clearly seen. The specific humidity tracer displays less distinct structure as compared with the other two tracers (similar as that shown by Vérèmes et al., 2016). The cross-section of PV in Fig. 8a have demonstrated relatively finer-scale structure of the stratospheric PV intrusions (below the jet stream), which penetrated down deeply into ~650 hPa (~3.6 km).

3.4. Trajectory model analysis

Figure 9 shows 30h backward trajectories ending at the radar site at 18 UT 29 November (left panel) and at 18 UT 30 November (right panel). As expected, the air masses parcel transported eastward horizontally before the occurrence of main

306 downdrafts (fig.10a). Whereas after the downdrafts, the trajectories clearly show that
307 the tropospheric air masses over the radar site are of stratospheric origin from the
308 western side of Lake Baikal. Trajectory results further support the evidence of
309 stratospheric intrusions that closely related with the main downdrafts.

310 On the other hand, 30-h forward trajectories starting at 00 UT 30 November (left
311 panel) and 00 UT 1 December (right panel) are shown in Fig. 10. It is interesting to note
312 that, from Fig.11a before the passage of COL, the air parcels at 4 km transport rapidly
313 upward (by more than 4 km within ~23 h) and northeastward to the upper-troposphere
314 of East Siberian. This upward and poleward transportation is associated with a warm
315 conveyor belt (southerly flows dominate) that is located ahead of the COL. It
316 contributes to transporting the tropospheric moist and polluted air (such as aerosol) into
317 the upper-troposphere and even the lower stratosphere (e.g. Stohl et al., 2003; Sandhya
318 et al., 2015). After the downdrafts, forward trajectories in fig.11b demonstrate that the
319 dry intrusion air parcels continue to be transported downward and southeastward to the
320 boundary layer or even the surface.

321 3.5. Strong downdrafts preceding rapid tropopause ascent and discussion

322 Figure 11a shows another 20 typical cases of strong downdrafts preceding rapid
323 RT ascent for the period Mar. 2012 and Jan. 2015 (shown placed end-to-end), the LRT
324 height (plotted in crosses) and the vertical velocity of the RT (plotted in orange line) is
325 also plotted. These cases (marked by black rectangular boxes and labeled as S1, S2,
326 S3…, and S20) are identified based on the following criteria: 1) the amplitude of the
327 RT ascent should exceed 0.6 km (four range gates), 2) vertical velocities of the RT

328 ascent excess 0.1 km/h, 3) the downdrafts occurred preceding the RT ascent should >0.5
329 m/s, and the height region of the downdrafts should pass through the RT layer. The
330 criteria are put forward mainly to avoid the influence of the RT spikes. Figure 11b
331 shows the backward trajectories for the selected 9 cases. Results show clear evidence
332 of downward intrusions corresponding to the associated strong downdrafts. Their
333 sources are mainly from West Siberia (western side of Lake Baikal), except for the case
334 Tr5. Moreover, according to AIRS daily 500 hPa ozone distribution, most of the cases
335 in Figure 11a (except for the cases S14, S15, S16, S17, S20) were associated with
336 significant ozone enhancement, indicating intrusions of stratospheric origin (as shown
337 in Supplementary figure S1). It is important to note that the RT excursion velocity of
338 all the cases is not all above 0.2 km/h and some are lower than this value (e.g. cases
339 S16 and S18). However, some form of stratospheric intrusions was exactly observed in
340 such cases from both the trajectory and satellite results. Therefore, the threshold of
341 vertical velocity of the RT ascent is set at 0.1 km/h, rather than 0.2 km/h (Hocking et
342 al., 2007). Large differences between RT and LRT are also interesting to be noted on
343 some occasions when the RT changes rapidly (such as the occasion near 14 Mar. 2012).
344 According to the meteorological chart, the synoptic situation of those cases
345 identified in Fig. 11a are introduced. The cases S1, S2, S8, S9, S10, and S11 seem to
346 have a close relationship with COL development; cases S3, S4, S5, S6, S7, S17, S18,
347 and S19 seem associated with low or high trough systems (at 500 hPa). The remaining
348 cases seem not associated with any significant synoptic development. However, in
349 terms of the distribution of isentropic PV (generally at 315K in winter and 330K in

summer), we found that the remaining cases S12, S13, S14, S15, S16, and S20 appear to be associated with some form of stratospheric streamers and their break-up within the previous 48h (not shown). Some cases (e.g. S1 and S2) that appear close on the same day were probably caused by the same system. The characteristics of the 20 cases, including background synoptic condition, vertical velocity of the RT ascent, and 500 hPa ozone enhancement, have been summarized in Table 2.

In the light of present understanding, the strong downdrafts preceding the rapid RT ascent can serve as an important diagnostic for intrusion events, during various synoptic processes in any season. This characteristic will be of great use and play an important role in routine identification of stratospheric intrusions. Considering the duration of such downdrafts, a higher time resolution of radar observations will be more helpful. Present study has shown the duration of the majority downdrafts is generally within 1.5-3 hours. We consider, therefore, that the radar resolution should be best within 1h.

Although Hocking et al. (2007) have reported that the rapid tropopause ascent (>0.2 km/h) alone can be a useful diagnostic for potential intrusion events. However, using only the information of RT heights might lead to non-negligible errors, as mentioned above in introduction and according to the observations in Fig. 11. Especially on occasions when the RT ascent is between 0.1-0.2 km/h but the corresponding true intrusions were observed, all such intrusion events will be neglected (maybe ~2 per month, refer to Fig. 12a). Whereas on some occasions when the RT ascent exceeds 0.2 km/h, but without observing true intrusion events (e.g. He et al.,

372 2011), these events will be misdiagnosed (maybe ~13 per month, refer to Fig. 12b). In
373 this sense, using the unique MST radar observations of both the RT height variability
374 and the vertical wind as complementary signature for identifying possible intrusion
375 events is very meaningful.

376 Figure 12 shows four years (2012-2015) of the events with rapid RT ascent (gray
377 bands), and the events with strong downdrafts just preceding the rapid RT ascent (black
378 bands). The identification criteria of such strong downdrafts are similar to that
379 mentioned above and the events are classified according to different value of vertical
380 velocity of the ascent. Among all the events with ascent velocity between 0.1-0.2 km/
381 h, about one-quarter (approximate 2 per month, Fig. 12a) were observed with strong
382 downdrafts preceding them. Whereas, as for the events with the ascent velocity >0.2
383 km/h, the proportion is about a half (approximate 10 per month, Fig. 12b). Here,
384 according to the results above, the occurrence of the strong downdrafts just preceding
385 the rapid RT ascent (black bands in Fig. 12) to a large degree represents the occurrence
386 of possible intrusions. In this way, Fig. 12 indicates that the occurrence of possible
387 intrusions exhibit distinct seasonal variations, with a maximum in winter and spring
388 minimum in summer. This is because the meso- and small-scale atmospheric processes,
389 such as cold air outbreaks, thunderstorms, and convective activities, are more active in
390 winter and spring. They are important sources for downward stratospheric intrusions.
391

4. Conclusions

Detailed case analysis of the cross-tropopause stratospheric intrusions was carried out during a COL. Global reanalysis, satellite data, and HYSPLIT trajectories all showed consistent evidences of dry ozone-rich, high PV, and depleted CH4 air that have penetrated downward into the free troposphere. The key signature of the stratospheric intrusions in the Beijing MST radar observations is the strong downdrafts just preceding rapid RT ascent. The radar echo power decreased rapidly within the region of strong downdrafts, after which abnormal high aspect sensitivity was recorded in troposphere. Such high aspect sensitivity is served as another potential clue for the intrusions of stratospheric origin.

Based on the criteria mentioned in section 3.5, other 20 typical cases of strong downdrafts preceding the rapid RT ascent between Mar. 2012 and Jan. 2015 were presented. These events occurred during different synoptic processes in different seasons. Yet, most of the cases (15 of them) are associated with some form of intrusions observed by combination of AIRS-retrieved ozone and the HYSPLIT trajectory model. Our results show that the radar-derived tropopause height and vertical winds are strong complementary indicators to be used to infer the occurrence of the intrusions of stratospheric origin. This will be of great use and play an important role for the routine identification or prediction of intrusion events. However, the actual origin of the observed downdrafts preceding the rapid RT ascent is not addressed in this paper. Further combination observational experiments need to be conducted, especially combined using ozonesonde soundings, to quantitative analyze the effectiveness of

present identification criteria for possible intrusions.

Acknowledgment

The authors really appreciate Prof Shira Raveh-Rubin for reading and checking the manuscript, using the criterion in Raveh-Rubin, 2017. This work is funded by National Natural Science Foundation of China (NSFC grants No. 41722404 and 41474132). The authors would like to thanks the technical and scientific staff of Chinese Meridian Space Weather Monitoring Project (CMSWMP) for their support in conducting the experiment. The authors sincerely acknowledge the ECMWF, NASA, and NOAA Air Resources Laboratory (ARL) for providing global reanalysis, satellite trace gases, and HYSPLIT transport model, respectively. The MST radar data for this paper are available at Data Centre for Meridian Space Weather Monitoring Project (http://159.226.22.74/). The radiosonde data is available from http://weather.uwyo.edu/upperair/sounding.html.

References

Appenzeller, C., Holton, J. R., & Rosenlof, K. H.: Seasonal variation of mass transport across the tropopause. Journal of Geophysical Research Atmospheres, 101(D10), 15071–15078, 1996.

Appenzeller, C., Davies, H. C., & Norton, W. A.: Fragmentation of stratospheric intrusions. Journal of Geophysical Research Atmospheres. 101(D1), 1435-1456, 1996.

Alexander, S. P., Murphy, D. J., and Klekociuk, A. R.: High resolution VHF radar measurements of tropopause structure and variability at Davis, Antarctica (69° S, 78° E). Atmospheric Chemistry and Physics, 13(12), 26173-26205, 2012.

Bonasoni, P., Evangelisti, F., Bonafe, U., Ravegnani, F., Calzolari, F., Stohl, A., Tositti L., Tubertini O., & Colombo, T.: Stratospheric ozone intrusion episodes recorded at Mt. Cimone during the VOTALP project: case studies. Atmospheric Environment, 34(9), 1355-1365, 2000.

Butchart, N., Cionni, I., Eyring, V., Shepherd, T. G., Waugh, D. W., & Akiyoshi, H., et al.: Chemistry-climate model simulations of twenty-first century stratospheric climate and circulation changes. Journal of Climate, 23(20), 5349-5374, 2010.

Chipperfield, M. P., Bekki, S., Dhomse, S., Harris, N., Hassler, B., & Hossaini, R., et al.: Detecting recovery of the stratospheric ozone layer. Nature, 549(7671), 211-218, 2017.

Chen, P.,: Isentropic cross-tropopause mass exchange in the extratropics. Journal of Geophysical Research, 16661-16673, 1995.

452 Chen, G., Cui, X., Chen, F., Zhao, Z., Wang, Y., Yao, Q., ... & Gong, W.: MST Radars
453 of Chinese Meridian Project: System Description and Atmospheric Wind
454 Measurement. IEEE Transactions on Geoscience and Remote Sensing, 54(8),
455 4513-4523, 2016.
456 Das, S. S., A. R. Jain, K. K. Kumar, and D. Narayana Rao: Diurnal variability of the
457 tropical tropopause: Significance of VHF radar measurements, Radio Sci., 43,
458 RS6003, doi:10.1029/2008RS003824, 2008.
459 Das, S. S., Ratnam, M. V., Uma, K. N., Patra, A. K., Subrahmanyam, K. V., Girach, I.
460 A., Suneeth K. V. , Kumar K. K.,. & Ramkumar, G.:Stratospheric intrusion into
461 the troposphere during the tropical cyclone Nilam (2012). Quarterly Journal of the
462 Royal Meteorological Society, 142(698), 2168-2179, 2012.
463 Ding, A., and T. Wang: Influence of stratosphere-to-troposphere exchange on the
464 seasonal cycle of surface ozone at Mount Waliguan in western China, Geophysical
465 Research Letters, 33, L03803, doi.10.1029/ 2005GL024760, 2006.
466 Elbern, H., Kowol, J., Sládkovic, R., & Ebel, A.: Deep stratospheric intrusions: a
467 statistical assessment with model guided analyses. Atmospheric Environment,
468 31(19), 3207-3226, 2006.
469 Gage, K. S., & Green, J. L.: Tropopause detection by partial specular reflection with
470 Very-High-Frequency radar. Science, 203(4386), 1238-40, 1979.
471 Gerasopoulos, E., Zanis, P., Papastefanou, C., Zerefos, C.S., Ioannidou, A., Wernli, H.:
472 A complex case study of down to the surface intrusions of persistent stratospheric
473 air over the Eastern Mediterranean. Atmospheric Environment, 40(22), 4113-4125,

2006.

He, H., Tarasick, D. W., Hocking, W. K., Careysmith, T. K., Rochon, Y. J., Zhang, J., ... & Bourqui, M. S.: Transport analysis of ozone enhancement in Southern Ontario during BAQS-Met. Atmospheric Chemistry and Physics, 11(6), 2569-2583, 2011.

Hocking, W. K., Careysmith, T., Tarasick, D. W., Argall, P. S., Strong, K., Rochon, Y. J., Zawadzki Irek & Taylor, P. A.: Detection of stratospheric ozone intrusions by windprofiler radars. Nature, 450(7167), 281-284, 2007.

Holton, J. R., P. H. Haynes, M. E. McIntyre, A. R. Douglass, R. B. Rood, and L. Pfister: Stratosphere-troposphere exchange, Reviews of Geophysics, 33(4), 403–439, doi:10.1029/95RG02097, 1995.

Hoskins B.J., McIntyre M.E., Robertson A.W.: On the use and significance of isentropic potential vorticity maps. Q. J. R. Meteorol. Soc. 111: 877–946. 1985.

Hirschberg, P. A., and J. M. Fritsch: A study of the development of extratropical cyclones with an analytic model. Part I: The effects of stratospheric structure, Journal of the Atmospheric Sciences, 50, 311 –327, doi:10.1175/1520-0469(1993)050<0311:ASOTDO>2.0.CO;2, 1993.

Kim, K. E., Jung, E. S., Campistron, B., & Heo, B. H.: A physical examination of tropopause height and stratospheric air intrusion: a case study. Journal of the Meteorological Society of Japan, 79(5), 1093-1103, 2001.

Kumar, K. K., & Uma, K. N.: High temporal resolution VHF radar observations of stratospheric air intrusions in to the upper troposphere during the passage of a mesoscale convective system over gadanki (13.5° n, 79.2° e). Atmospheric

Chemistry & Physics, 24(8), 14-17, 2009.

Kumar, K. K.: VHF radar observations of convectively generated gravity waves: Some new insights. Geophysical Research Letters, 33(1), doi:10.1029/2005GL024109, 2006.

Leclair de Bellevue J, Baray JL, Baldy S, Ancellet G, Diab R, Ravetta F.: Simulations of stratospheric to tropospheric transport during the tropical cyclone Marlene event. Atmospheric Environment. **41**: 6510–6526, doi: 10.1016/j.atmosenv.2007.04.040, 2007.

Lefohn, A. S., Wernli, H., Shadwick, D., Limbach, S., Oltmans, S. J., Shapiro, M.: The importance of stratospheric–tropospheric transport in affecting surface ozone concentrations in the western and northern tier of the United States. Atmospheric Environment, 45(28), 4845-4857, 2011.

Mahlman, J. D.: Dynamics of transport processes in the upper troposphere. Science, 276(5315), 1079-1083, 1997.

Mihalikova, M., Kirkwood, S., Arnault, J., & Mikhaylova, D.: Observation of a tropopause fold by MARA VHF wind-profiler radar and ozonesonde at Wasa, Antarctica: comparison with ECMWF analysis and a WRF model simulation. Annales Geophysicae, 30(9), 1411-1421, 2012.

Monks, P. S.: A review of the observations and origins of the spring ozone maximum, Atmospheric Environment, 34, 3545–3561, 2000.

Nastrom, G. D., Green, J. L., Gage, K. S., & Peterson, M. R.: Tropopause folding and the variability of the tropopause height as seen by the flatland VHF radar. Journal

518 of Applied Meteorology, 28(12), 1271-1281, 1989.
519 Oltmans, S. J., and H. Levy II.: Seasonal cycle of surface ozone over the western North
520 Atlantic, Nature, 358, 392–394, 1992.
521 Ottersten, H.: Mean vertical gradient of potential refractive index in turbulent mixing
522 and radar detection of CAT, Radio Science, 4, 1247–1249,
523 doi:10.1029/RS004i012p01247, 1969.
524 Price, J. D., & Vaughan, G.: The potential for stratosphere-troposphere exchange in cut-
525 off-low systems. Quarterly Journal of the Royal Meteorological Society, 119(510),
526 343-365, 1993.
527 Rao, T. N., and S. Kirkwood: Characteristics of tropopause folds over Arctic latitudes,
528 Journal of Geophysical Research, 110, D18102, doi:10.1029/2004JD005374,
529 2005.
530 Rao, T. N., Arvelius, J., & Kirkwood, S.: Climatology of tropopause folds over a
531 european arctic station (esrange). Journal of Geophysical Research Atmospheres,
532 113(D7), 762-770, 2008.
533 Ravindrababu, S., Venkat Ratnam, M., Sunilkumar, S. V., Parameswaran, K., and
534 Krishna Murthy, B. V.: Detection of tropopause altitude using Indian MST radar
535 data and comparison with simultaneous radiosonde observations. Journal of
536 Atmospheric and Solar-Terrestrial Physics, 121(6), 679-687, 2014.
537 Ramaswamy V, Schwarzkopf MD, Shine KP.: Radiative forcing of climate from
538 halocarbon-induced global stratospheric ozone loss. Nature **355**: 810–812, doi:
539 10.1038/355810a0, 1992.

Rolph, G.D.: Real-time Environmental Applications and Display sYstem (READY) Website. NOAA Air Resources Laboratory, Silver Spring, MD. http://www.arl.noaa.gov/ready/hysplit4.html, 2003.

Sandhya, M., Sridharan, S., & Indira Devi, M.: Tropical upper tropospheric humidity variations due to potential vorticity intrusions. Annales Geophysicae, 33(9), 1081-1089, 2015.

Skerlak, B., Sprenger, M., Pfahl, S., Tyrlis, E., & Wernli, H.: Tropopause folds in ERA-Interim: Global climatology and relation to extreme weather events. Journal of Geophysical Research, 120(10), 4860-4877, 2015.

Stohl, A., Bonasoni, P., Cristofanelli, P., Collins, W., Feichter, J., & Frank, A., et al.: Stratosphere-troposphere exchange: a review, and what we have learned from staccato. Journal of Geophysical Research Atmospheres, 108(D12), 469-474, 2003.

Stohl, A., et al.: The influence of stratospheric intrusions on alpine ozone concentrations, Atmospheric Environment, 34, 1323– 1354, 2000.

Stohl, A., Wernli, H., James, P., Bourqui, M., Forster, C., & Liniger, M. A., et al.: A new perspective of stratosphere troposphere exchange. Bulletin of the American Meteorological Society, 84(11), 2003.

Stein, A. F., Draxler, R. R., Rolph, G. D., Stunder, B. J. B., Cohen, M. D., & Ngan, F.: Noaa's HYSPLIT atmospheric transport and dispersion modeling system. Bulletin of the American Meteorological Society, 96(12), 150504130527006, 2016.

Stevenson, D. S., Dentener, F. J., Schultz, M. G., Ellingsen, K., Noije, T. P. C. V., &

562 Wild, O., et al.: Multimodel ensemble simulations of present-day and near-future
563 tropospheric ozone. Journal of Geophysical Research Atmospheres, 111(D8), 263-
564 269, 2006.
565 Sørensen, J. H., and Nielsen, N. W.: Intrusion of stratospheric ozone to the free
566 troposphere through tropopause folds -a case study. Physics and Chemistry of the
567 Earth Part B Hydrology Oceans and Atmosphere, 26(10), 801-806, 2001.
568 Su, L., Yuan, Z., Fung, J. C., & Lau, A. K.: A comparison of HYSPLIT backward
569 trajectories generated from two GDAS datasets. Science of The Total Environment,
570 527-537, 2015.
571 Susskind, J., C. D. Barnet, and J. M. Blaisdell.: Retrieval of atmospheric and surface
572 parameters from AIRS/AMSU/HSB data in the presence of clouds, IEEE
573 Transactions on Geoscience and Remote Sensing, 41(2), 390–409,
574 doi:10.1109/tgrs.2002.808236, 2003.
575 Vaughan, G., Gouget, H., O'Connor, F. M., & Wier, D.: Fine-scale layering on the edge
576 of a stratospheric intrusion. Atmospheric Environment, 35(12), 2215–2221, 2001.
577 Vérèmes, H., J.-P. Cammas, J.-L. Baray, P. Keckhut, C. Barthe, F. Posny, P. Tulet, D.
578 Dionisi, and S. Bielli: Multiple subtropical stratospheric intrusions over Reunion
579 Island: Observational, Lagrangian, and Eulerian numerical modeling approaches,
580 Journal of Geophysical Research Atmospheres, 121, 14,414–14,432, doi:10.1002/
581 2016JD025330, 2016.
582 Wang, C.: New Chains of Space Weather Monitoring Stations in China. Space Weather-
583 the International Journal of Research and Applications, 8(8), 2010.

584 World Meteorological Organization (WMO): Atmospheric ozone 1985, WMO Global
585 Ozone Res. and Monit. Proj. Rep. 20, Geneva, Switzerland, 1986.
586 Xiong, X., C. Barnet, E. Maddy, S. C. Wofsy, L. Chen, A. Karion, and C. Sweeney.:
587 Detection of methane depletion associated with stratospheric intrusion by
588 atmospheric infrared sounder (AIRS), Geophysical Research Letters, 40, 2455–
589 2459, doi:10.1002/grl.50476, 2013.
590 Yamamoto, M., Oyamatsu, M., Horinouchi, T., Hashiguchi, H., & Fukao, S.: High time
591 resolution determination of the tropical tropopause by the Equatorial Atmosphere
592 Radar. Geophysical Research Letters, 30(21), 2003.
593

Table

Radar parameter	Value
Transmitted frequency	50 MHz
Antenna array	24×24 3-element Yagi
Antenna gain	33 dB
Transmitter peak power	172.8 kW
Code	16-bit complementary
No. coherent integrations	128
No. FFT points	256
No. spectral average	10
Pulse repetition period	160 μs
Half power beam width	3.2^o
Pulse length	1 μs
Range resolution	150 m
Temporal resolution	30 min
Off-zenith angle	15^o

Table 1. Operating parameters in low-mode of the Beijing MST radar.

Cases	Time (year/month/day)	Background condition	Vertical velocity of RT ascent	500 hPa ozone enhancement
S1	2012/03/06	Cut-off low	>0.2 km/h	Enhanced
S2	2012/03/06	Cut-off low	>0.2 km/h	Enhanced
S3	2012/03/12	Low/high trough	>0.2 km/h	Enhanced
S4	2012/03/13	Low/high trough	>0.2 km/h	Enhanced
S5	2012/04/05	Low/high trough	>0.2 km/h	Enhanced
S6	2012/04/05	Low/high trough	>0.2 km/h	Enhanced
S7	2012/04/06	Low/high trough	>0.2 km/h	Enhanced
S8	2012/06/13	Cut-off low	>0.2 km/h	Enhanced
S9	2012/06/13	Cut-off low	>0.2 km/h	Enhanced
S10	2013/08/02	Cut-off low	>0.2 km/h	Enhanced
S11	2013/08/02	Cut-off low	>0.2 km/h	Enhanced

S12	2013/08/03	PV streamer	>0.2 km/h	Enhanced
S13	2013/08/03	PV streamer	>0.2 km/h	Enhanced
S14	2014/01/02	PV streamer	>0.2 km/h	None
S15	2014/01/02	PV streamer	>0.2 km/h	None
S16	2014/01/03	PV streamer	0.1-0.2 km/h	None
S17	2014/01/04	Low/high trough	>0.2 km/h	None
S18	2014/05/02	Low/high trough	0.1-0.2 km/h	Enhanced
S19	2014/05/02	Low/high trough	>0.2 km/h	Enhanced
S20	2015/01/03	PV streamer	>0.2 km/h	None

597 **Table 2.** Characteristics of the 20 cases shown in Fig. 11a.

598

Figures

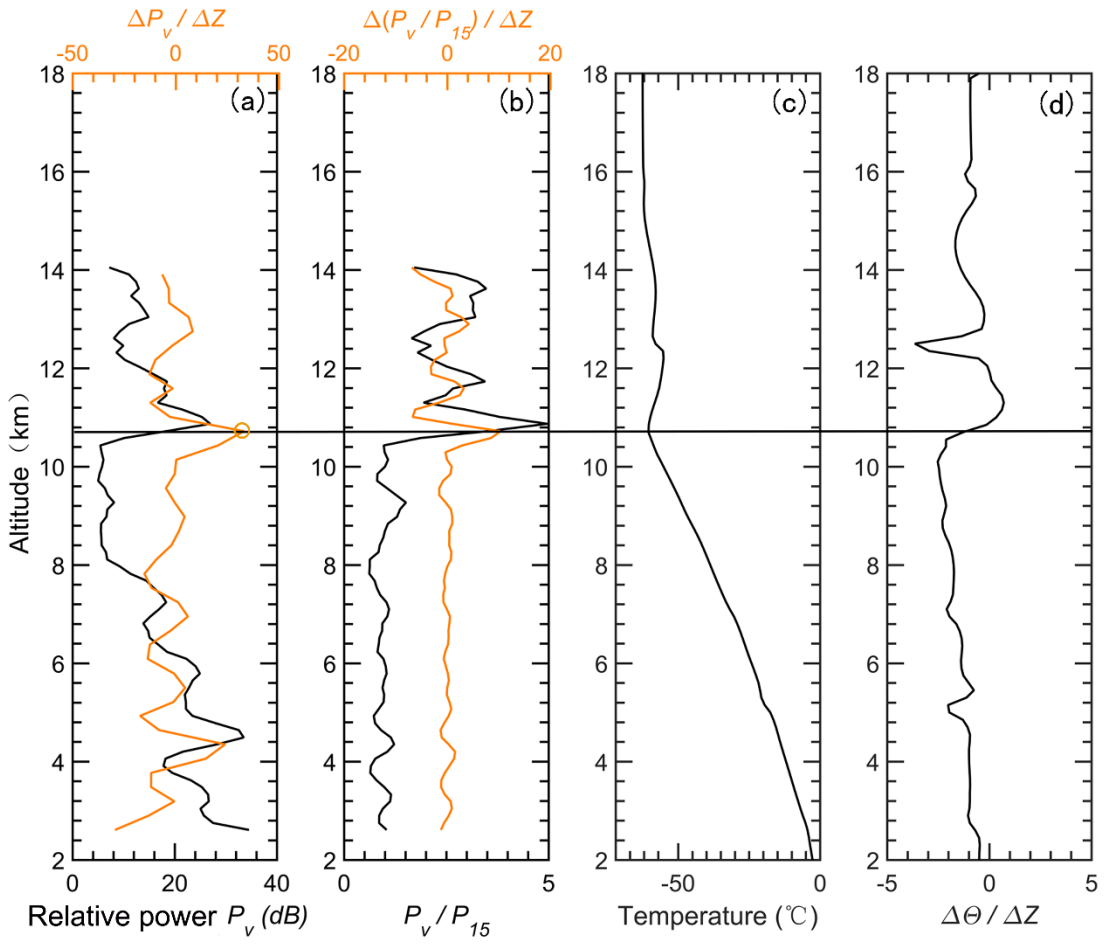

Figure 1. Example of the vertical height profiles of (a) the relative radar echo power (black line, smoothed by a 3-point running mean) along with its gradient variation (orange line), (b) the aspect sensitivity (black line, expressed as the ratio between the vertical echo power and oblique echo power) along with its gradient variation (orange line), observed on 12 UT 29 November 2014. The vertical profiles of simultaneous radiosonde observed temperature and potential temperature gradient are shown in plots (c) and (d). The black horizontal line denotes the LRT height derived from the radiosonde temperature profile. The orange circle indicates the RT height derived from the profile of the radar backscattered echo power.

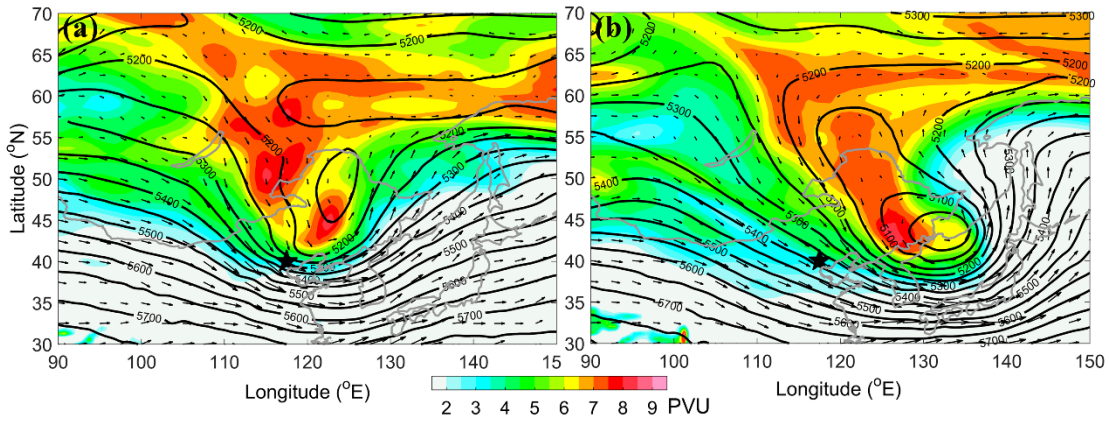

610

611 **Figure 2.** ECMWF derived isentropic PV map on 315 K surface (shaded above 2 pvu,

612 1 PVU=10^{-6} m^2 K kg^{-1} s^{-1}) and geopotential height (contoured every 50 m in solid line)

613 along with the wind vector (arrow) at 500 hPa (~5.5 km a.s.l.) on (a) 18 UTC 30

614 November 2014, (b) 12 UTC 1 December 2014. The black star shows the location of

615 Xianghe.

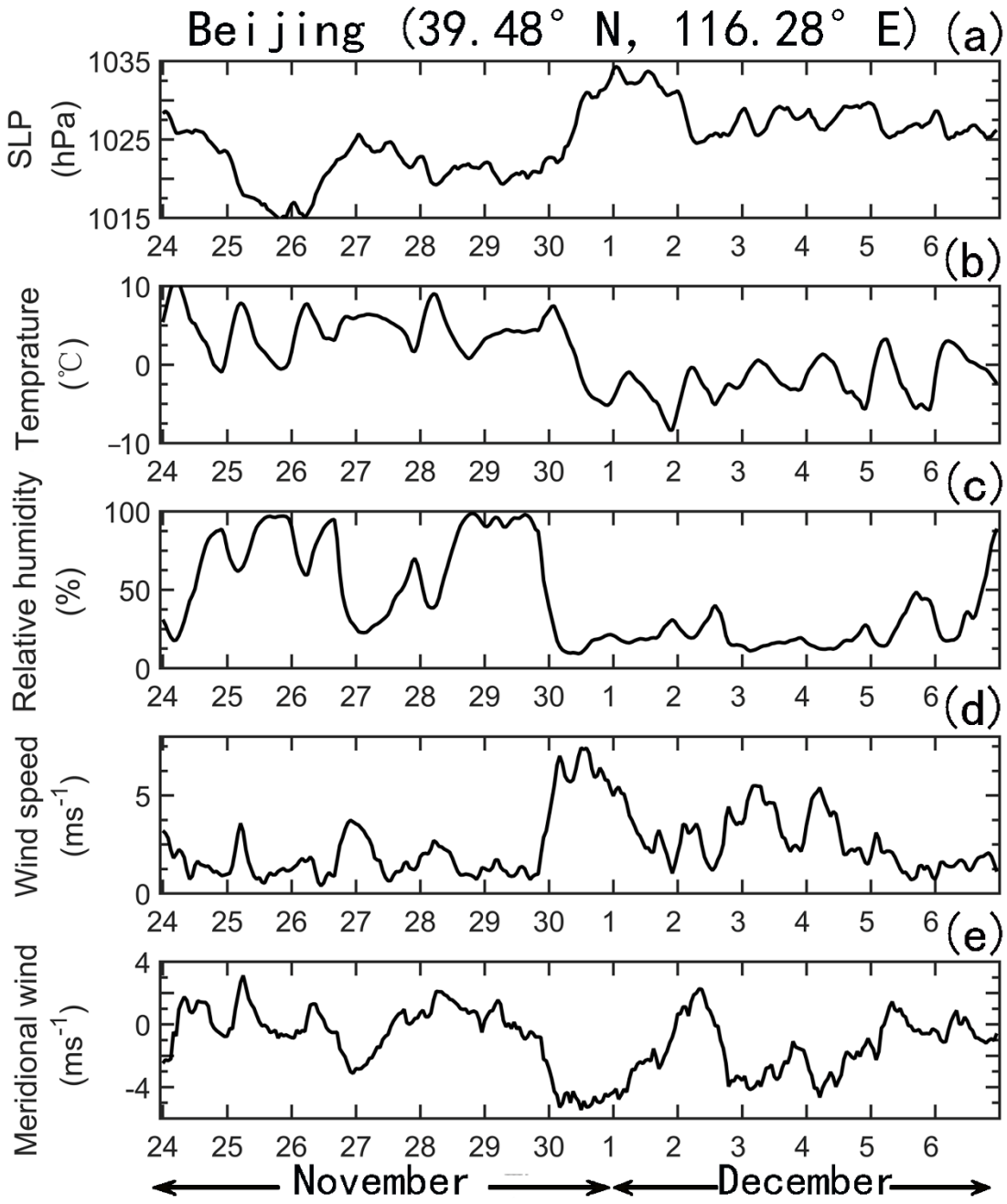

616

617 **Figure 3.** Time series of surface (~1.2 m above the surface) hourly meteorological
618 measurements of (a) sea level pressure, (b) temperature, (c) relative humidity, (d)
619 horizontal wind, and (e) meridional wind during the period 24 Nov.-6 Dec. 2014,
620 observed over the Beijing station (39.4° N, 116.2° E, 31.3 m above sea level).

621

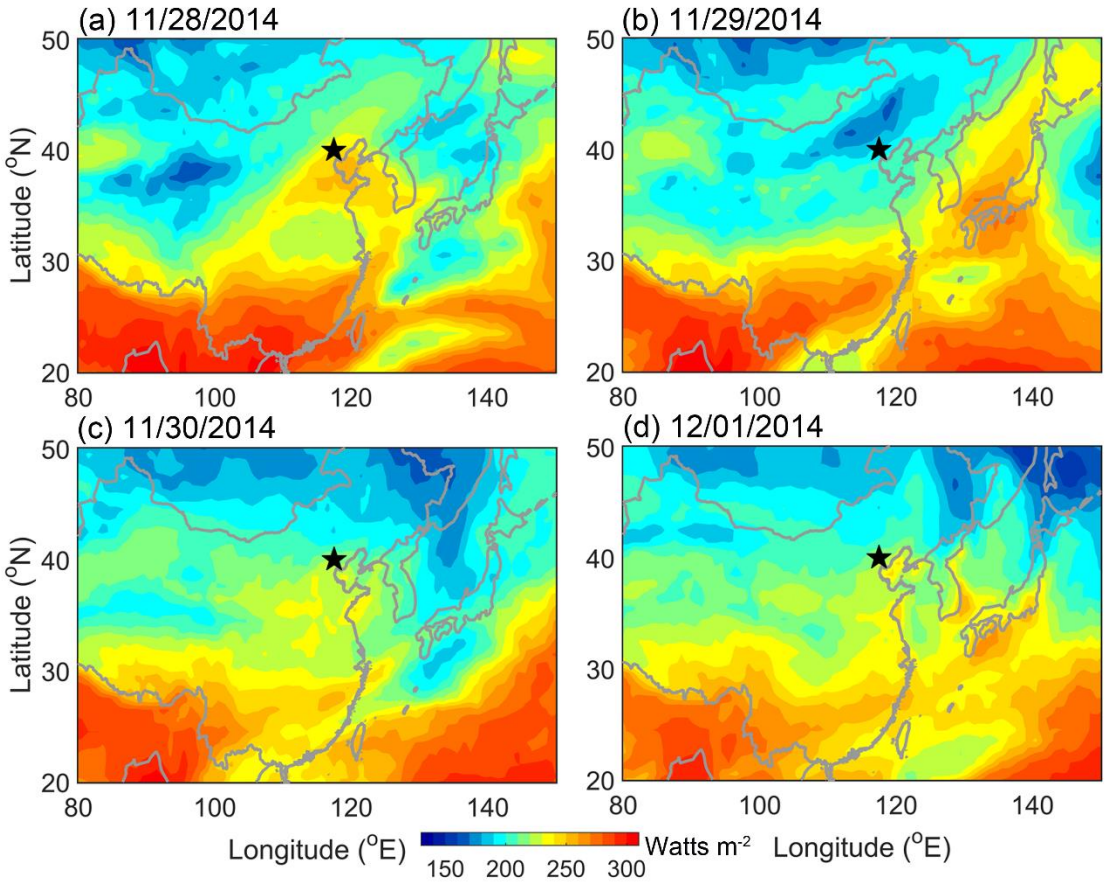

622

623 **Figure 4.** Contour maps of the high quality Climate Data Record (CDR) of the daily
624 Outgoing Longwave Radiation (OLR), derived from the NOAA high-resolution
625 infrared radiation sounder (HIRS) on (a) 28 Nov., (b) 29 Nov., (c) 30 Nov., and (d) 1
626 Dec. 2014. The black star shows the location of Xianghe.

627

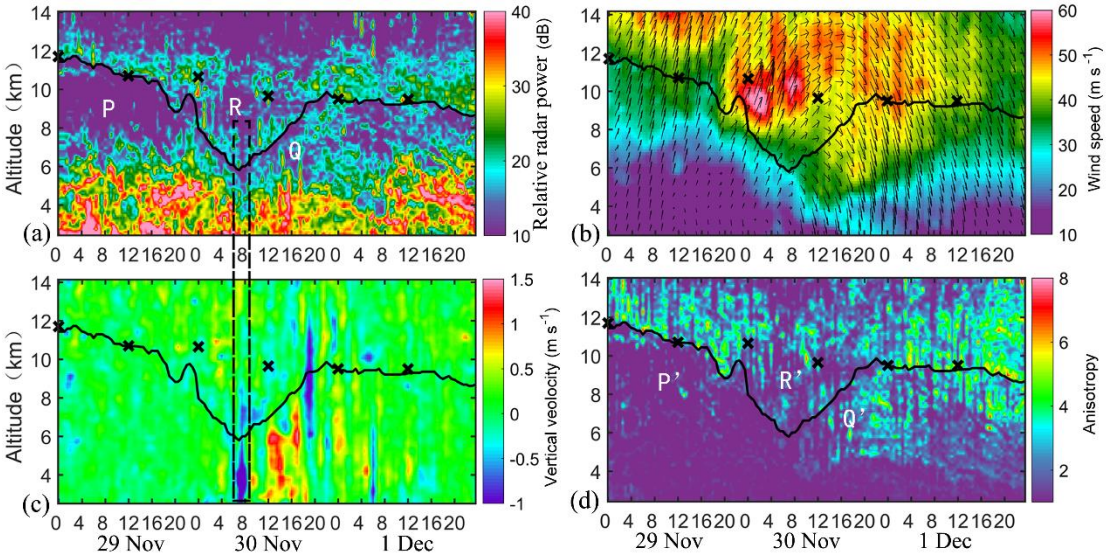

628

629 **Figure 5.** Altitude-time section of (a) the radar backscattered echo power in zenith
630 direction, (b) the horizontal wind speed along with wind vector, of which the up and
631 down arrows represent north and south respectively, and left-right is west-east, (c) the
632 vertical velocity, and (d) the aspect sensitivity, observed by the Beijing MST radar from
633 29 November to 1 December 2014. The black curve shows the radar-determined
634 tropopause, as defined in section 2.1. The dotted rectangle highlights the strong
635 downdrafts immediately preceding the rapid tropopause ascent. The positions of the
636 LRT tropopause heights, derived from the nearly simultaneous collocated GPS
637 radiosonde temperature profile, are marked by crosses.

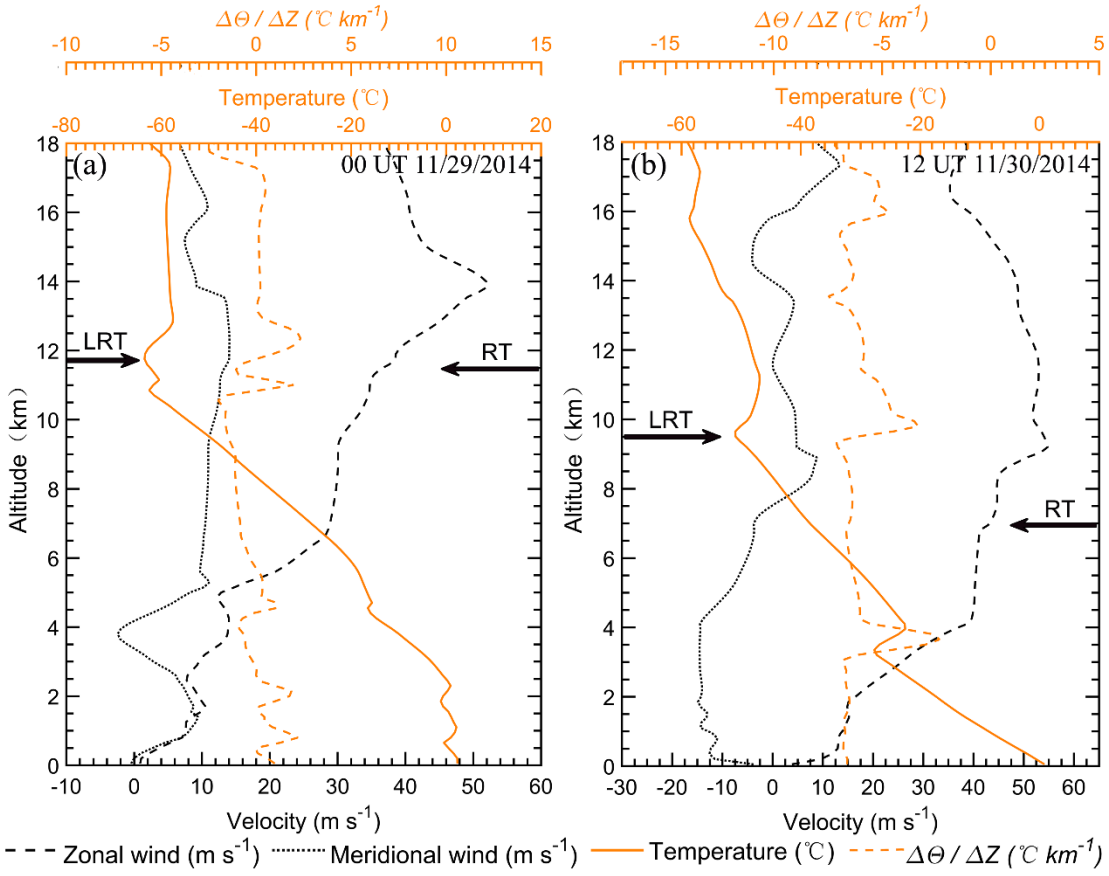

638

639 **Figure 6.** Vertical profiles of zonal wind, meridional wind, temperature, and potential

640 temperature gradient derived from the GPS radiosonde measurements, at (a) 0000 UTC

641 29 November 2014 and (b) 1200 UTC 30 November 2014. The bold arrows on the left

642 and right side of each panel indicate the radiosonde derived LRT tropopause and radar-

643 derived tropopause height, respectively.

644

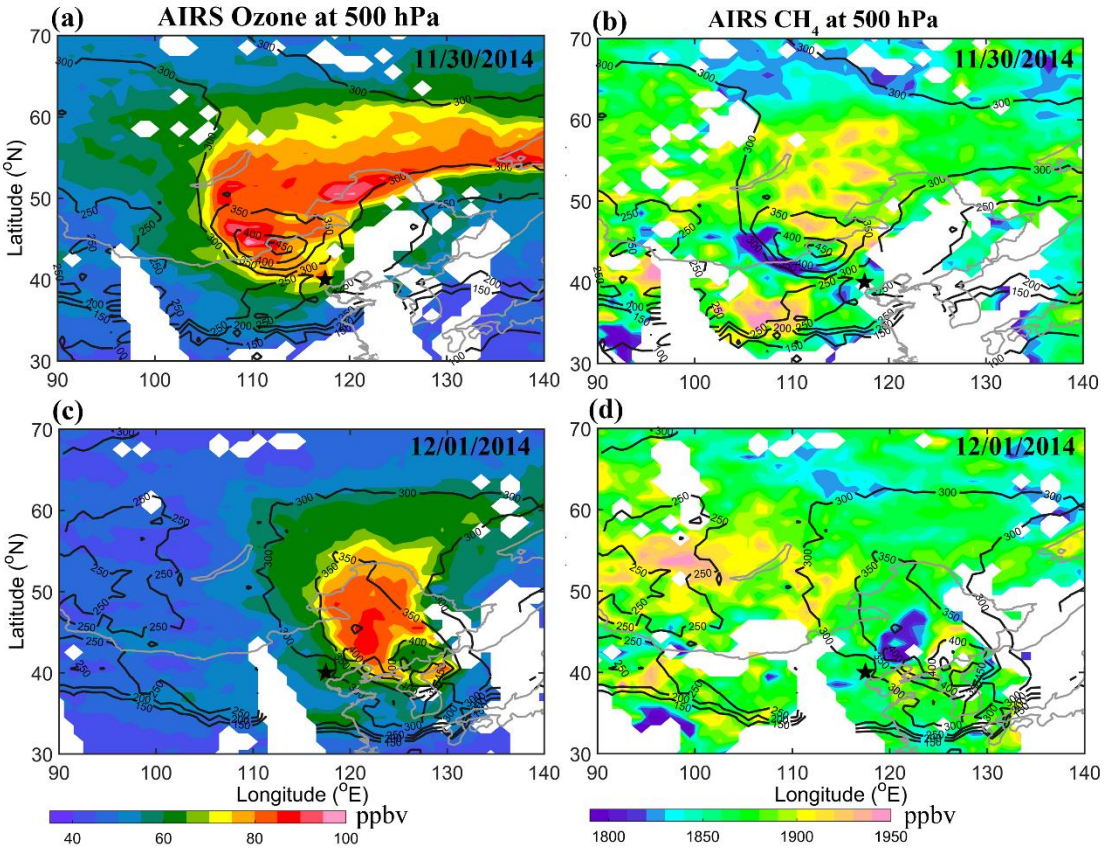

645

646 **Figure 7.** 500 hPa Ozone (left panels) and methane CH_4 (right panels) distribution

647 along with the tropopause height contour, derived from the AIRS satellite observations.

648 The top and bottom plots show the data of 30 Nov. 2014 and 1 Dec. 2014, respectively.

649 According to the Aqua Orbit Tracks (not shown), the time range of the satellite passage

650 is between ~04:00-07:25 on 30 November and between ~03:15-06:35 on 1 December

651 2014. The black star indicates the location of Xianghe.

652

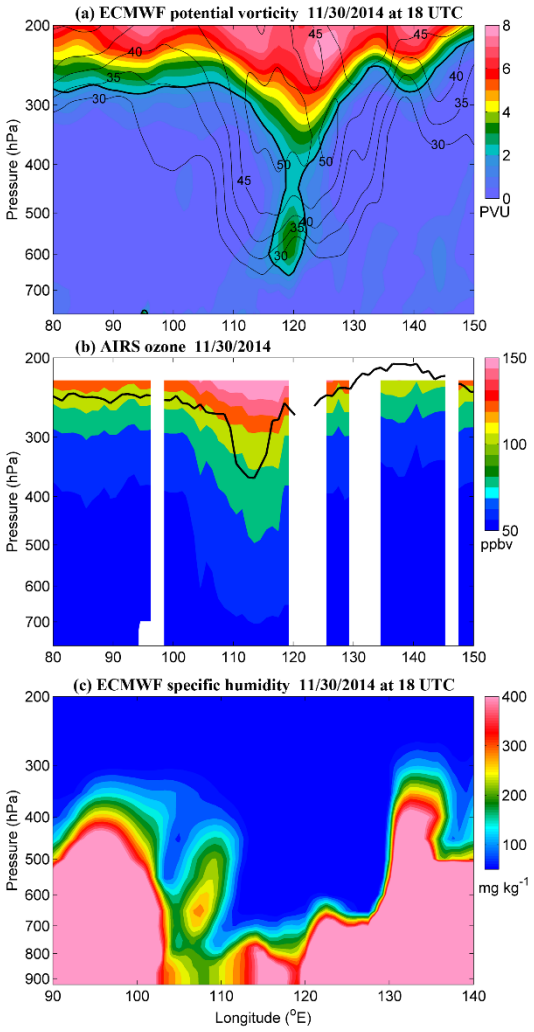

653

654 **Figure 8.** Longitude-pressure cross section of (a) ECMWF PV (colors, in pvu) along

655 with horizontal wind contour (thin black line, m/s) at 18 UTC on 30 Nov. 2014, (b)

656 AIRS ozone mixing ratio (colors, in ppbv) along with tropopause height (black line) on

657 30 Nov. 2014, and (c) ECMWF specific humidity (colors, in mg kg^{-1}) at 18 UTC on 30

658 Nov. 2014, at a constant latitude 40° N (nearest grid point in the latitude of Xianghe).

659 The bold line in (a) marks the isotropic line of PV at 2 pvu.

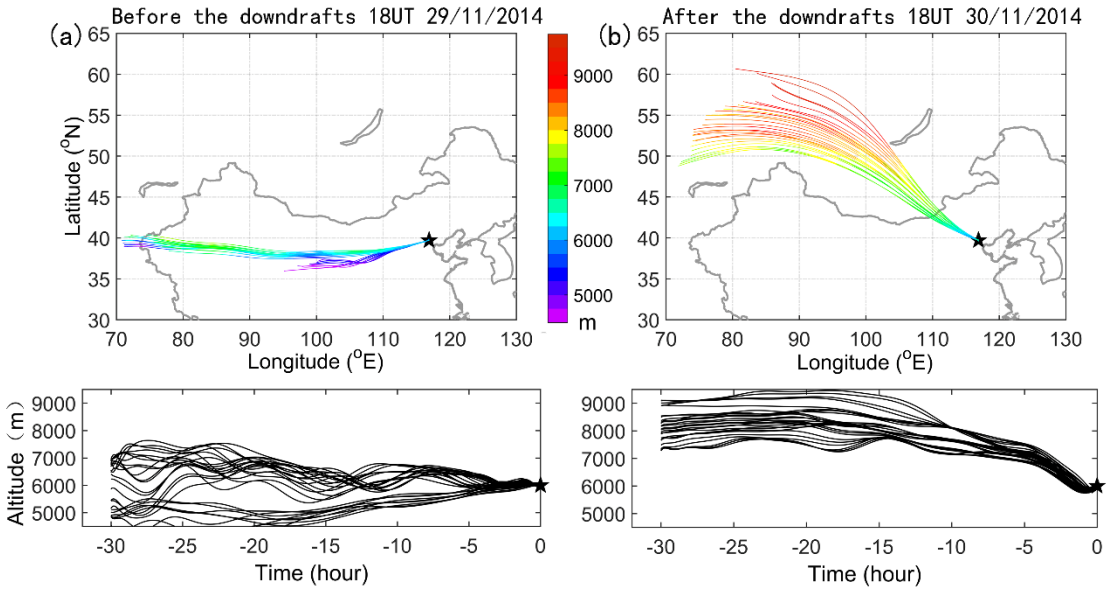

660

661 **Figure 9.** Illustration of 30 h three-dimensional backward trajectories ending at
662 Xianghe at 6000 m using National Oceanic Atmospheric Administration (NOAA)
663 HYSPLIT model: (a) before the main downdrafts at 18 UTC on 29 November 2014,
664 and (b) after the main downdrafts at 18 UTC on 30 November 2014. The HYSPLIT
665 ensemble consists of 27 trajectories. Upper plots show the horizontal projection of the
666 trajectories, and the lower plots show the corresponding time-height vertical
667 displacement of the trajectories.

668

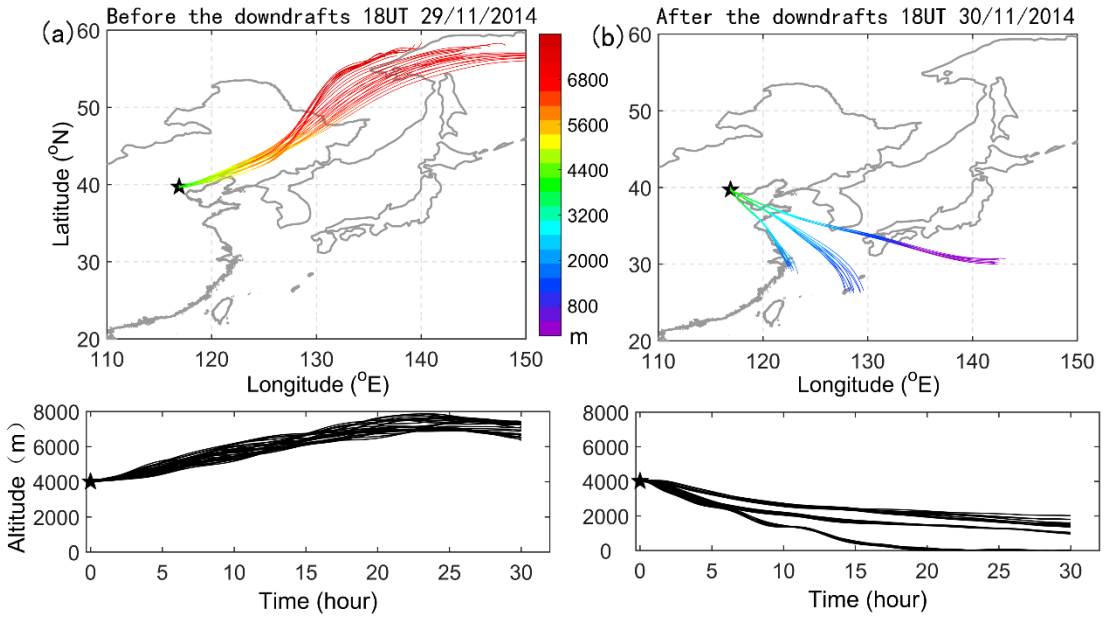

669

670 **Figure 10.** Same as Fig.10 but for three-dimensional forward trajectories starting at

671 Xianghe at 4000 m: (a) before the main downdrafts at 00 UTC on 30 November 2014,

672 and (b) after the main downdrafts at 00 UTC on 1 December 2014.

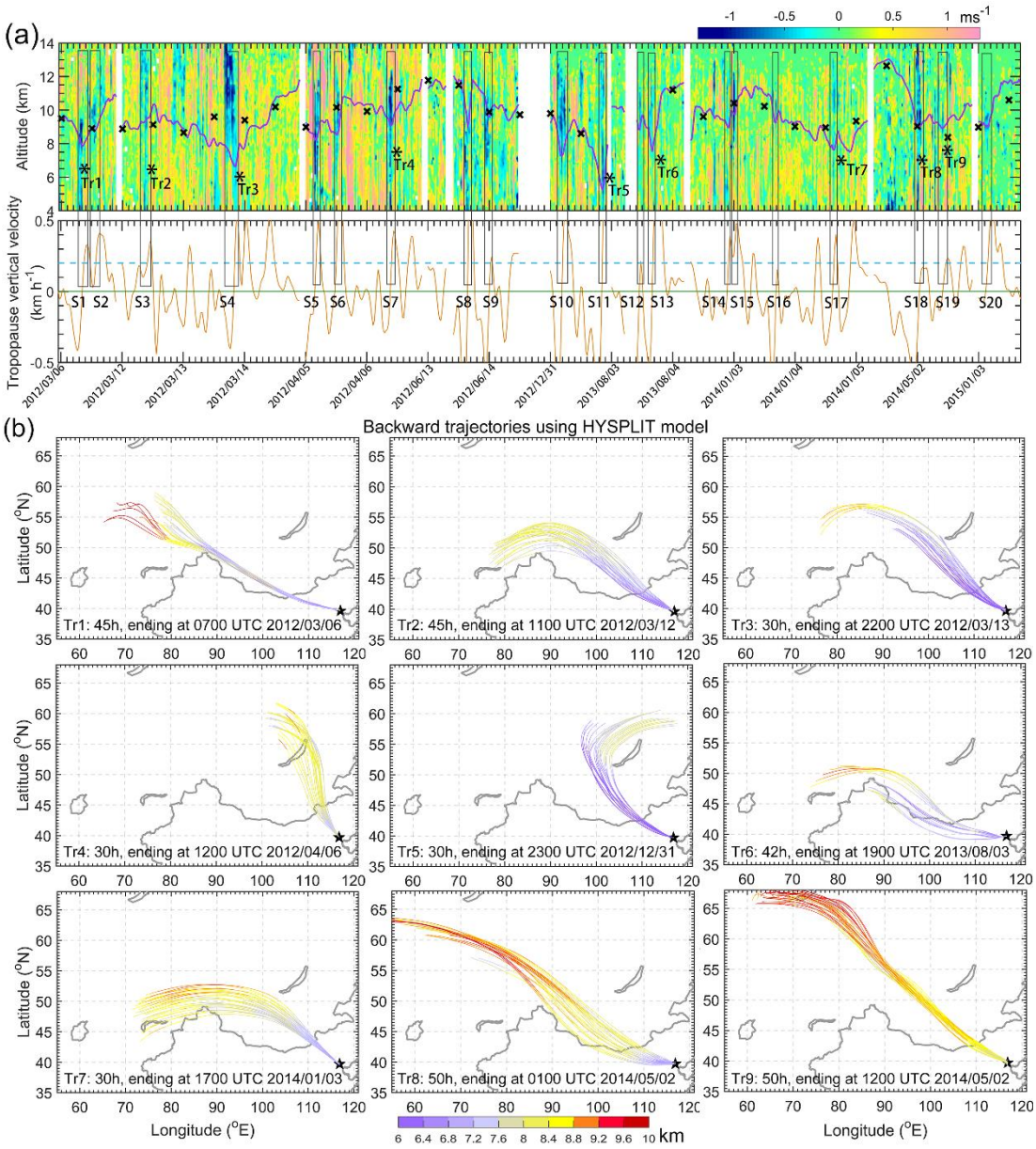

673

674 **Figure 11.** (a) Height-time section of several episodic observations of the radar-derived
675 vertical wind (colors in m/s) along with RT height (purple bold line) and LRT height
676 (bold crosses), between Mar. 2012 and Jan. 2015. The corresponding vertical velocity
677 of the RT (orange line) is plotted in the lower panel of (a), dotted blue line indicates the
678 value of 0.2 km/h. Dates for the observations are displayed as year/month/day. Black
679 rectangular boxes represent the cases of strong downdraughts (absolute value $\geqslant$0.5 m/s)
680 preceding rapid tropopause ascent (>0.1 km h^{-1}) and are labeled as S1, S2, S3…, S20.

681 Symbol '*' labeled as Tr1-Tr9 indicates the ending point of the corresponding
682 trajectories in Fig.12b. (b) Results of backward trajectories (colors in km) of the typical
683 9 selecting cases from Fig.12a, providing the signature and source of possible
684 stratospheric intrusions.
685

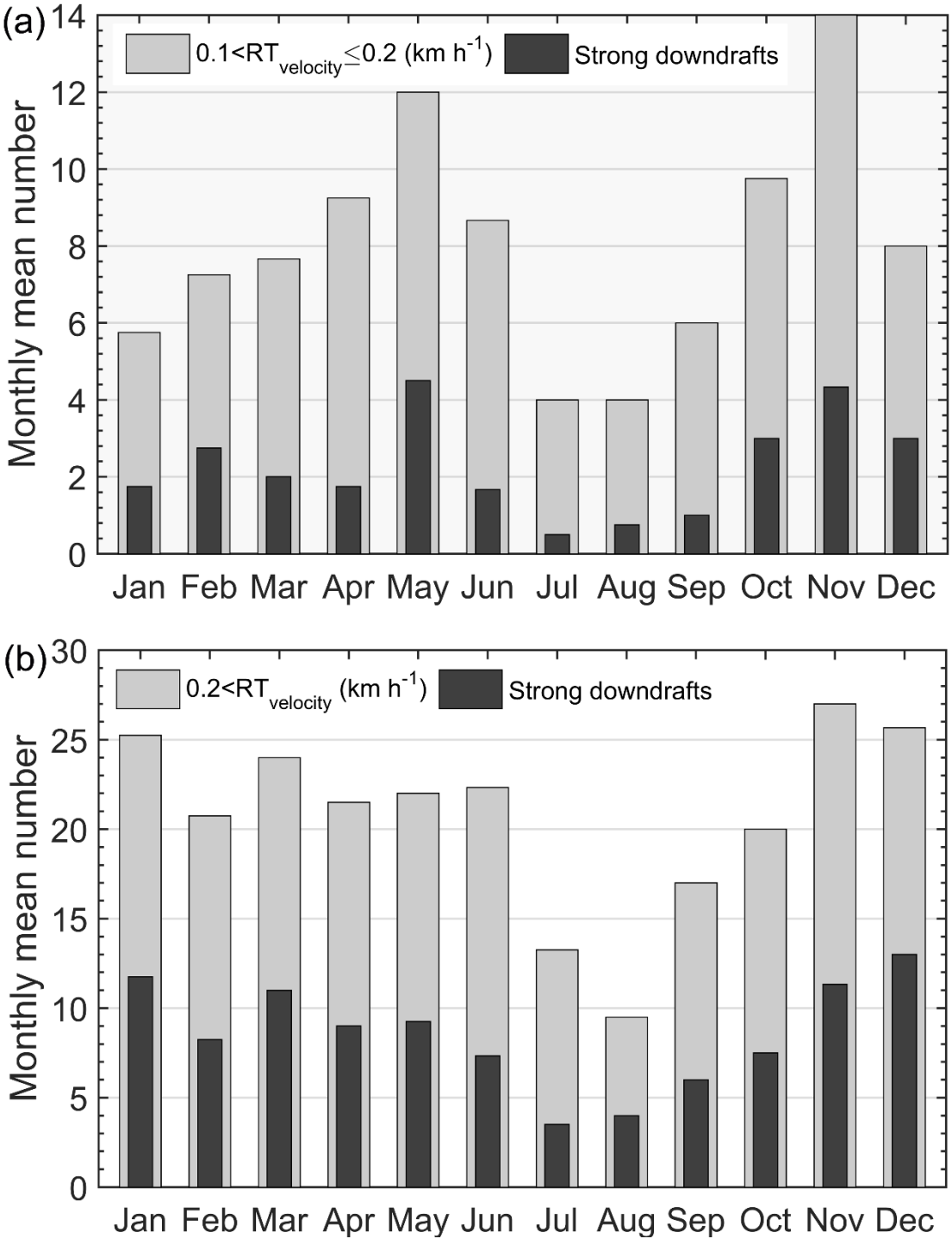

686

687 **Figure 12.** Four years (2012-2015) of radar-determined monthly mean number of rapid

688 tropopause ascent (gray bands) and the corresponding strong downdrafts just preceding

689 the rapid tropopause ascent (black bands). (a) Gray bands: with the ascent by at least

690 0.6 km and the excursion velocity is between 0.1-0.2 km h^{-1}; black bands: except for

691 the criteria of gray bands, strong downdrafts occurred preceding the rapid RT ascent

must exceed 0.5 m s^{-1} and pass through the RT layer. (b) Same as (a) but for the occasions when the ascent velocity is larger than 0.2 km h^{-1}. According to the study here, the black bands in the histogram well represent the occurrence of possible stratospheric intrusions.